AGU PUBLICATIONS

JGR

Journal of Geophysical Research: Solid Earth

RESEARCH ARTICLE
10.1002/2017JB014141

Key Points:
- Full wavefield decomposition is applied to short-period secondary microseisms recorded in 2013 at the Pilbara spiral array in NW Australia
- Rayleigh and Love waves are observed at distinct, differing azimuths
- The vertical/transverse ratio in microseismic energy decreases with increasing frequency and is strongly direction and frequency dependent

Supporting Information:
- Supporting Information S1

Correspondence to:
M. Gal,
martin.gal@utas.edu.au

Citation:
Gal, M., A. M. Reading, S. P. Ellingsen, K. D. Koper, and R. Burlacu (2017), Full wavefield decomposition of high-frequency secondary microseisms reveals distinct arrival azimuths for Rayleigh and Love waves, *J. Geophys. Res. Solid Earth*, *122*, 4660–4675, doi:10.1002/2017JB014141.

Received 25 FEB 2017
Accepted 4 JUN 2017
Accepted article online 11 JUN 2017
Published online 28 JUN 2017

Full wavefield decomposition of high-frequency secondary microseisms reveals distinct arrival azimuths for Rayleigh and Love waves

M. Gal[1], A. M. Reading[1], S. P. Ellingsen[1], K. D. Koper[2], and R. Burlacu[2]

[1]School of Physical Sciences, University of Tasmania, Hobart, Tasmania, Australia, [2]Geology and Geophysics, University of Utah, Salt Lake City, Utah, USA

Abstract In the secondary microseism band (0.1–1.0 Hz) the theoretical excitation of Rayleigh waves (R_g/*LR*), through oceanic wave-wave interaction, is well understood. For Love waves (*LQ*), the excitation mechanism in the secondary microseism band is less clear. We explore high-frequency secondary microseism excitation between 0.35 and 1 Hz by analyzing a full year (2013) of records from a three-component seismic array in Pilbara (PSAR), Australia. Our recently developed three-component waveform decomposition algorithm (CLEAN-3C) fully decomposes the beam power in slowness space into multiple point sources. This method allows for a directionally dependent power estimation for all separable wave phases. In this contribution, we compare quantitatively microseismic energy recorded on vertical and transverse components. We find the mean power representation of Rayleigh and Love waves to have differing azimuthal distributions, which are likely a result of their respective generation mechanisms. Rayleigh waves show correlation with convex coastlines, while Love waves correlate with seafloor sedimentary basins. The observations are compared to the WAVEWATCH III ocean model, implemented at the Institut Français de Recherche pour l'Exploitation de la Mer (IFREMER), which describes the spatial and temporal characteristics of microseismic source excitation. We find Love wave energy to originate from raypaths coinciding with seafloor sedimentary basins where strong Rayleigh wave excitation is predicted by the ocean model. The total power of R_g waves is found to dominate at 0.35–0.6 Hz, and the Rayleigh/Love wave power ratio strongly varies with direction and frequency.

Plain Language Summary We focus on the continuous seismic background energy that has its origin in the oceans. Contrary to earthquakes, this seismic energy is generated by ocean wave processes as continuous earth vibrations. The origin and composition of the wavefield is well understood for acoustic and vertically polarized surface waves but less clear for transversely polarized surface waves. We make use of a spiral seismic array northwest of Australia and decompose the continuous seismic wavefield into its fundamental polarization and energy contributions. This allows us to study which geographical regions generate a certain type of seismic wave, and measure the energy and temporal variation of the signal. We find that contrary to previous beliefs, vertically and transversely polarized seismic waves are not observed from the same directions with the seismic array but show distinct arrival directions. We are able to correlate the transversely polarized seismic waves to regions with sedimentary basins.

1. Introduction

Ambient noise studies in the range of 0.05–1 Hz have predominantly focused on the analysis of Rayleigh (LR/R_g) [e.g., *Friedrich et al.*, 1998; *Shapiro and Campillo*, 2004; *Chevrot et al.*, 2007; *Kedar et al.*, 2008; *Roux*, 2009; *Schimmel et al.*, 2011; *Reading et al.*, 2014] and *P* waves [e.g., *Gerstoft et al.*, 2008; *Zhang et al.*, 2009; *Landès et al.*, 2010; *Traer et al.*, 2012; *Euler et al.*, 2014; *Gal et al.*, 2015]. The excitation mechanisms of Rayleigh (*LR*, Rayleigh wave; R_g, high-frequency crustal Rayleigh wave) and *P* waves are well understood in primary microseisms (direct coupling of gravity waves in sloping shallow bathymetry [*Haubrich et al.*, 1963]) and in secondary microseisms (oceanic wave-wave interaction [*Longuet-Higgins*, 1950; *Hasselmann*, 1963]). Numerical models [*Kedar et al.*, 2008; *Ardhuin et al.*, 2011; *Ardhuin and Roland*, 2012] correlate well with observations [e.g., *Stutzmann et al.*, 2012; *Obrebski et al.*, 2013; *Koper and Burlacu*, 2015].

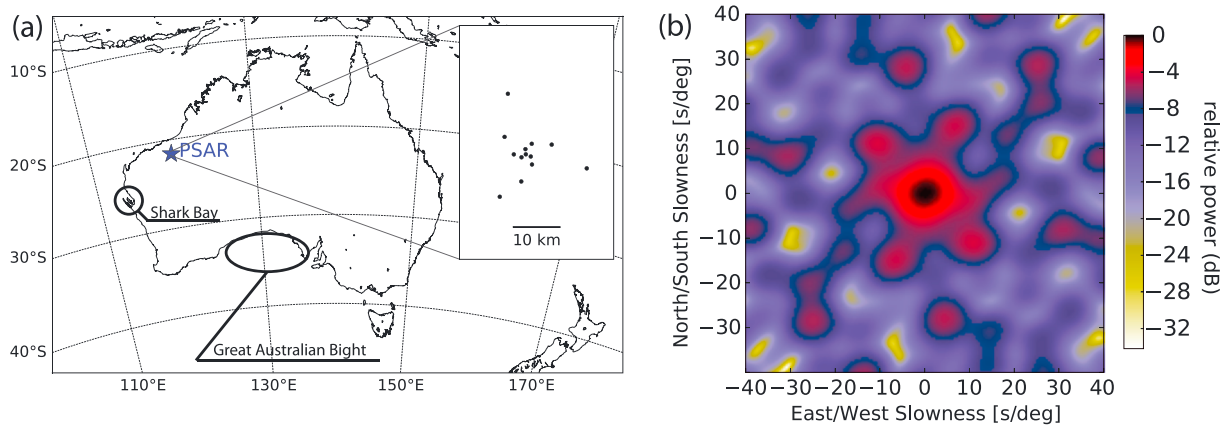

Figure 1. (a) Geographical location and array geometry are shown with (b) the corresponding array response function at 0.6 Hz.

Transversely polarized energy in the form of Love waves (*LQ*) [*Toksöz and Lacoss*, 1968; *Haubrich and McCamy*, 1969; *Roueff et al.*, 2009], L_g [*Koper et al.*, 2009, 2010], and SH body waves [*Liu et al.*, 2016; *Nishida and Takagi*, 2016] is also present in microseisms. The generation mechanisms of these phases in the secondary microseism band (defined here as 0.1–1.0 Hz) are not fully understood. The L_g phase (supercritical *S* waves trapped in the crustal waveguide), predominantly observed in high-frequency microseisms [*Koper et al.*, 2010], is thought to be generated by topographic or bathymetric scattering of other wave types such as R_g [e.g., *He et al.*, 2008; *Gal et al.*, 2015]. While *LQ* generation in the primary microseism band (0.05–0.1 Hz) is related to shear traction of ocean waves on the sea bottom topography [*Saito*, 2010], in the secondary band the excitation mechanism is less clear. Recent observations show that the back azimuth of the strongest *LR* and *LQ* waves is approximately the same [*Nishida et al.*, 2008; *Hadziioannou et al.*, 2012; *Behr et al.*, 2013; *Juretzek and Hadziioannou*, 2016]. The power ratio between secondary microseism *LR* and *LQ* waves show differing results between three-component array beamforming studies [*Friedrich et al.*, 1998; *Nishida et al.*, 2008; *Juretzek and Hadziioannou*, 2016], which suggest that *LR* dominates over *LQ*, and ring laser studies [*Tanimoto et al.*, 2015, 2016], which suggest the opposite. However, this discrepancy could be of pure geographical nature, as *LR*/*LQ* ratios vary for different regions [*Juretzek and Hadziioannou*, 2016].

In this work, we utilize the capabilities of the deconvolution-enhanced three-component beamforming [*Gal et al.*, 2016] to decompose the high-frequency secondary microseismic wavefield as a function of polarization, back azimuth, velocity, and frequency. The analysis is carried out with a spiral-shaped array, composed of broadband three-component sensors, which is ideal for an omnidirectional study of the seismic wavefield. Our analysis allows for a bias-free assessment of beam power, which we use to estimate the mean power distribution of R_g, *LQ*, and L_g waves for the full year 2013. We then compare ratios of vertical and transverse energy as a function of velocity, back azimuth, and frequency to gain insight on the generation mechanisms of R_g, *LQ*, and L_g waves.

2. Data and Methods

The wavefield decomposition is carried out on microseismic data recorded at the Pilbara Array (PSAR) in northwestern Australia (Figure 1a). This analysis requires a horizontally isotropic velocity field within the array footprint to ensure plane wave propagation over a broad frequency range and high signal coherence for all stations. PSAR fulfills these conditions over the frequency range of 0.35–1 Hz. The array is composed of 13 broadband three-component (3C) stations in a spiral configuration with an aperture of 22.6 km. The spiral shape leads to a delta-like function array response (Figure 1b) with strong sidelobe suppression [*Kennett et al.*, 2015]. Additional information on the array response function for multiple frequency bands and surface wave energy from all directions can be found in Figure S1. The instrument response of the seismometers (type: KS2000, 120 s) is flat over the range of 0.02–10 Hz, and all time series are divided by the system (instrument and digitizer) gain to transform the raw data to ground velocity (m/s).

For the wavefield analysis, we make use of the deconvolution-enhanced CLEAN-3C Capon beamformer [*Gal et al.*, 2016]. The integration of deconvolution into the beamforming process is aimed at the removal of beam

sidelobe power, which occurs due to the finite number of seismic sensors and can result in a smeared power spectrum. In the presence of multiple contemporaneous sources, the beam sidelobes can lead to a power spectrum that does not represent the true power distribution of the observed wavefield. CLEAN-3C iteratively removes a fraction of the power of the strongest source, which simultaneously removes its sidelobe contribution. Hence, the spectrum is iteratively decomposed into point sources and the contribution of the beam sidelobes is removed. To calculate the beam power on all three components, we first calculate the polarization covariance matrix *Wagner and Owens* [1996]

$$\mathbf{Y}_{3C} = \mathbf{e}^{H}(\mathbf{k})\mathbf{C}_{3C}^{-1}(f)\mathbf{e}(\mathbf{k}) \tag{1}$$

where $\mathbf{C}_{3C}^{-1}(f)$ denotes the inverse cross spectral matrix, H is the conjugate transpose, f is the frequency, $\mathbf{k}$ is the wave number, and $\mathbf{e}$ denotes the steering matrix

$$\mathbf{e}(\mathbf{k}) = \begin{bmatrix} a_{Z1} & \dots & a_{ZD} & 0 & \dots & 0 & 0 & \dots & 0 \\ 0 & \dots & 0 & a_{N1} & \dots & a_{ND} & 0 & \dots & 0 \\ 0 & \dots & 0 & 0 & \dots & 0 & a_{E1} & \dots & a_{ED} \end{bmatrix}^{T}. \tag{2}$$

The steering matrix is a construct of three orthogonal steering vectors a_{xy}, where the subscript x denotes the component (vertical, north-south, east-west) and y the station number for D stations. In the usual case where vertical and horizontal sensors are at the same location, we have $\mathbf{a}_Z = \mathbf{a}_N = \mathbf{a}_E$. The resulting polarization matrix describes the power and polarization characteristics of the array beam for a specific wave number $\mathbf{k}$. The power is obtained via an eigenvalue decomposition of $\mathbf{Y}_{3C}(\mathbf{k})$ and is given as

$$P_{3C}(\mathbf{k}) = \sum_{n=1,2,3} \frac{1}{\lambda_n(\mathbf{k})} \left|\mathbf{u}_n(\mathbf{k})\right|^2, \tag{3}$$

where $\lambda_n(\mathbf{k})$ are the eigenvalues and $\mathbf{u}_n(\mathbf{k})$ the eigenvectors. Given that $\mathbf{Y}_{3C}(\mathbf{k})$ is a 3×3 matrix, the particle motion is decomposed into three unique polarization states. Each polarization state is defined by its corresponding eigenvector and its contribution is given by the eigenvalue. In general, the largest eigenvalue denotes the dominant polarization characteristic present in $\mathbf{Y}_{3C}(\mathbf{k})$. Since we make use of the Capon beamformer, which inverts the three-component cross spectral matrix, the smallest eigenvalue represents the strongest polarization. Here we make use of the two smallest eigenvalues only, as the third is in general dominated by noise and using all three eigenvalues would not improve our results but increase the noise level of the power spectrum.

The extension to CLEAN-3C is implemented by removing a fraction of power from the strongest source. This is achieved by directly modifying the cross spectral matrix, by removing a fraction ϕ of phase information associated with the strongest source $P_{3C}^{\max}$

$$\mathbf{C}_{3C}^{i+1} = \mathbf{C}_{3C}^{i} - \phi P_{3C}^{\max}\mathbf{e}(\mathbf{k}_{\max})\mathbf{e}^{H}(\mathbf{k}_{\max}), \tag{4}$$

where the wave number $\mathbf{k}_{\max}$ maximizes $P_{3C}(\mathbf{k}_max) = P_{3C}^{\max}$. By running multiple iterations, the power spectrum is "cleaned" and the final result is given as the sum over M iterations of the removed power

$$P_{\mathrm{CLN}}(\mathbf{k}) = \sum_{i}^{M} \phi P_{3C,i}^{\max}. \tag{5}$$

The iterative approach is needed to extract the accurate source powers from the beam map. In the case of multiple sources where the sidelobes interfere with each other, removal of the power spectrum maximum in one step would also remove sidelobe contributions induced by the other sources, i.e., an incorrect removal of energy and a successive bias in the beam map. By removing only a fraction of power, one also removes the sidelobe contribution of the strongest signal and hence reduces the bias on the other sources in the successive steps. A detailed derivation of the beamformer and the CLEAN-3C methodology can be found in *Gal et al.* [2016].

We process the full year 2013 of 3C PSAR data in three separate frequency bands: $f_1 = 0.35 \pm 0.0175$ Hz, $f_2 = 0.6 \pm 0.03$ Hz, and $f_3 = 1 \pm 0.05$ Hz. The idea is to study the wavefield over a broad frequency range, and the chosen frequency bands were selected with respect to PSARs resolution capabilities. The continuous data are divided into 1 h time windows, the mean of the time series is removed, and the Hann taper function

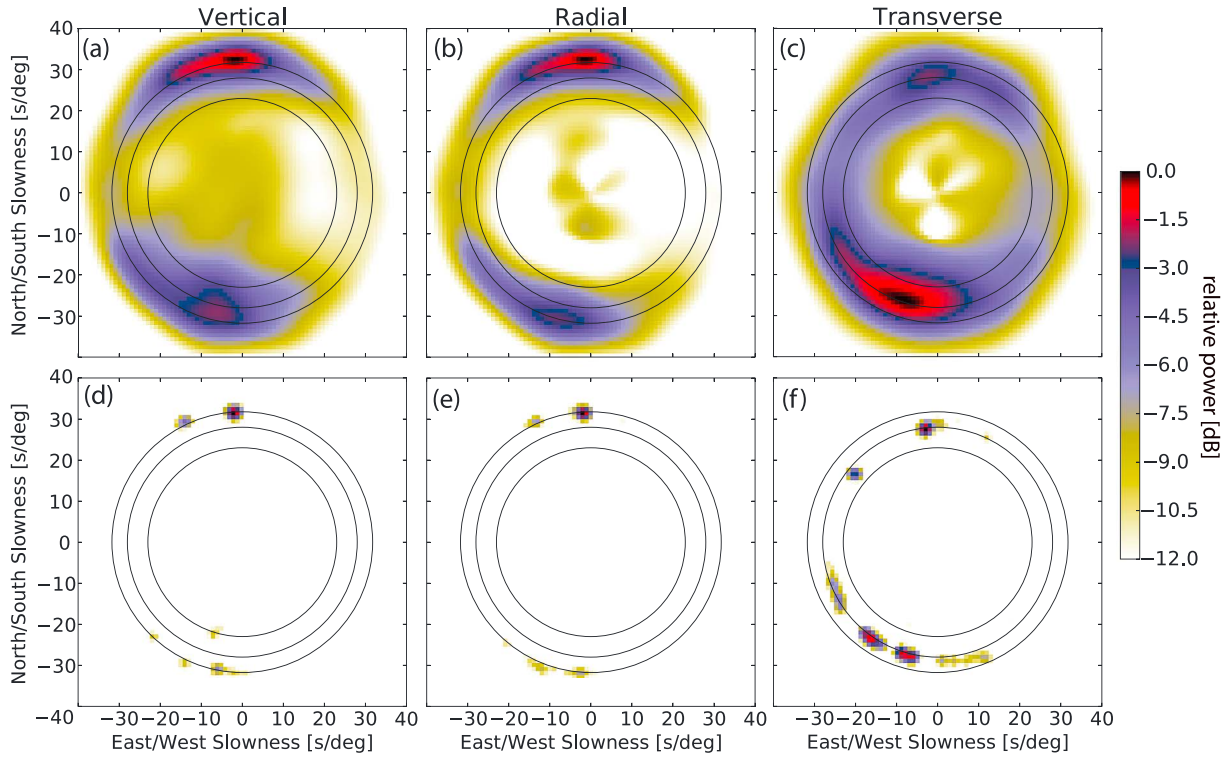

Figure 2. Beamforming power spectra for a 1 h long record, beginning on 2 January 2013 at 00:00:00 UTC, evaluated with 3C Capon beamforming at frequencies (f_1) of 0.35 ± 0.0175 Hz are shown. The power spectra are displayed for (a) *Z*, (b) *R*, and (c) *T* component data. The black circles of constant velocity are set at 3.4, 4.0, and 4.7 km/s. (d–f) The decomposition of the power spectra into point sources (convolved with a small Gaussian kernel to aid visibility). The decomposition of *Z* and *R* components shows identical results with the exception of the southern L_g arrival, which is only visible on the *Z* component. Both the high resolution of the array and the robustness of CLEAN-3C are evident. The power of cleaned sources is lower as the beam sidelobe bias is removed.

is applied to reduce spectral leakage. A time window overlap of 50% is used for each hour to compute the 3C power spectrum with the deconvolution-enhanced CLEAN-3C Capon beamformer [*Gal et al.*, 2016].

Using this new algorithm, each component (i.e., vertical (*Z*), radial (*R*), and transverse (*T*)) is evaluated and decomposed into separate point sources. The decomposition into point sources has the advantage that no sidelobe beam power is present, and a simple summation over all cleaned sources results in the total power of the given component. Alternatively, summation can be performed with bounds on azimuth and velocity to obtain directional power estimates for different phases. For a 1 h PSAR sample (Figures 2a–2c), the CLEAN-3C results are displayed in Figures 2d–2f.

A user-defined stopping criterion must be implemented in CLEAN-3C to achieve the optimal result. Of interest is the decomposition of the full power present in the cross spectral matrix and the avoidance of bias due to spurious features. The stopping criterion is determined as follows: in an initial frequency-dependent analysis, we estimate the phase velocities for R_g, L_g, and *LQ* waves with conventional 3C Capon beamforming [*Wagner and Owens*, 1996] using a month of data (January 2013). We find velocities of $R_g \sim 3.4$ km/s, $L_g \sim 4.0$–5.0 km/s on the *Z* component, and *LQ* ∼ 3.8–4.0 km/s on the *T* component. Acceptable velocity (*v*) bounds are then set to $3.0 < v < 5.5$ km/s, and, in the case of body waves, $v > 8.2$ km/s. Iterations of the CLEAN-3C procedure for the *Z* component are stopped once the beam power estimated from the residual phase information lies outside of the acceptable velocity bounds. The stopping criterion for the *R* component is identical to the *Z* component, while $3.3 < v < 5.5$ km/s applies for the *T* component. As we are interested in accurate power estimation of microseismic energy, we remove all earthquake related signals. This is achieved by inspecting the strongest cleaned source for each hour. In general, the power of the strongest source shows little change for adjacent hours and generates a smooth curve as a function of time. Strong earthquakes appear as outliers in this curve, and the cleaned sources associated with such behavior are removed from our results and all weaker microseism sources are retained in the analysis. Additionally, only results which passed at least 50 CLEAN-3C iterations are retained to avoid biased estimates.

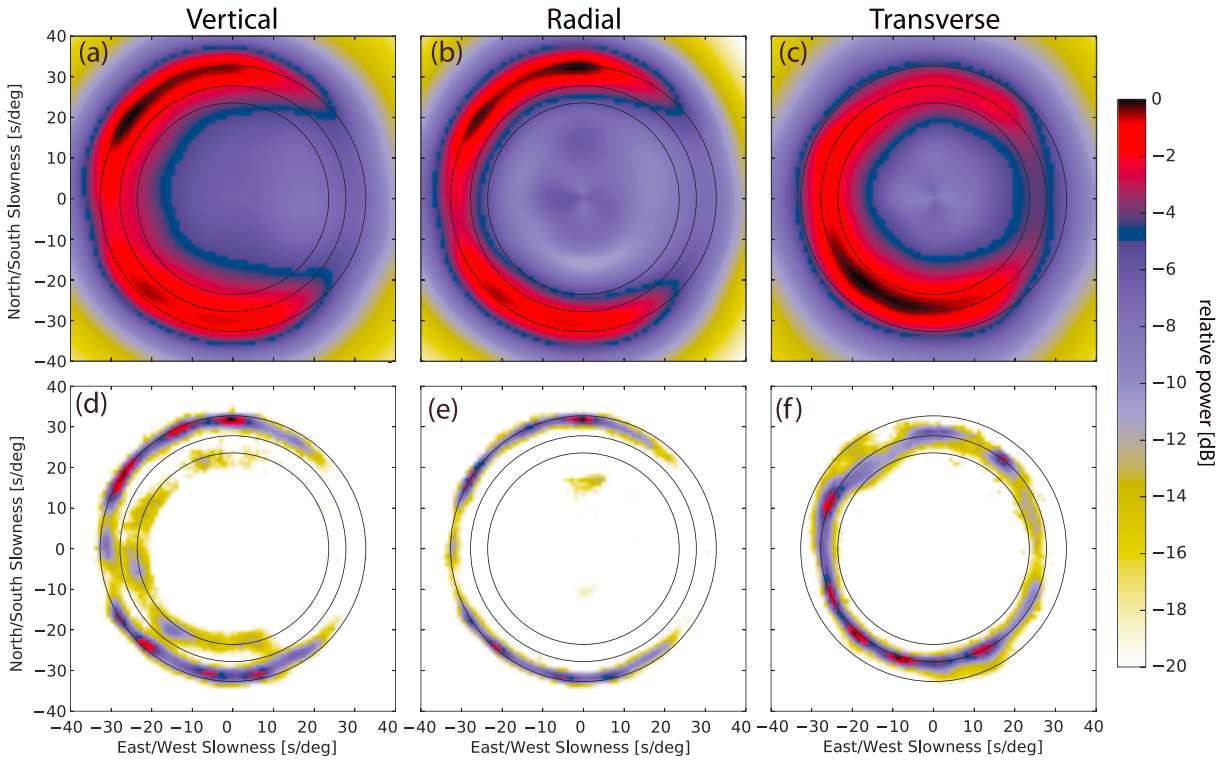

Figure 3. Summary plots for the full year 2013 for *Z*, *R*, and *T* components at $f_1 = 0.35 \pm 0.0175$ Hz. (a–c) The average power distribution estimated with the 3C-Capon beamformer [*Wagner et al.*, 1996]. (d–f) The mean power distribution derived with CLEAN-3C [*Gal et al.*, 2016]. The figures are generated by summing over all 1 h power spectra divided by the number of hours in a full year. The wavefield decomposition results in a sidelobe free power representation. Black circles of constant velocity follow the same convention as Figure 2.

In addition to these precautionary steps, we tested if spatially extended sources show signs of bias for the PSAR array configuration, given that CLEAN-3C removes point source energy. In a synthetic Monte Carlo approach, 10,000 configurations of randomly distributed spatially extended R_g and *LQ* sources were evaluated with CLEAN-3C. The sources were modeled with a phase velocity of 3.3 and 4.0 km/s, i.e., simulating R_g and *LQ* energy, and the azimuthal source extension varied randomly from 10 to 45°. The purpose of this test was to see if any directional bias due to spatially extended sources would occur, as the CLEAN-3C approach might not decompose extended sources accurately. The test did not show any directional preference due to the array configuration or power bias in the summary of the ten thousand synthetic wavefields. As an additional test, we modified the CLEAN-3C algorithm to remove energy distributed over an azimuth of 10° (for surface wave) instead of a point source and compared the results with the point source approach (Figure S2). The resulting mean power spectra were found to converge toward the point source solution and showed the same results (Figure S3).

3. Observations

The mean power representation of all three components analyzed with PSAR is summarized in Figure 3 and shows which parts of the slowness plane, i.e., back azimuth and velocity, are most active during the year 2013. We display the impact of deconvolution-enhanced CLEAN-3C beamforming with the help of two representations. Figures 3a–3c shows the mean power representation for the three components using the conventional 3C Capon approach *Wagner and Owens* [1996], and Figures 3d–3f displays the result with CLEAN-3C. In the first case, arrivals on all components are estimated from almost every azimuth with a relative power difference of 3 dB; i.e., the mean power representations suggest the power difference of surface waves to differ only by a factor of 2. In the case of CLEAN-3C, the beam sidelobes are removed and the mean power displays a strong variation with respect to direction and differences in relative power can be greater than 10 dB. Furthermore, the vertical component shows a higher velocity surface wave (L_g) to be present in the spectrum and the radial

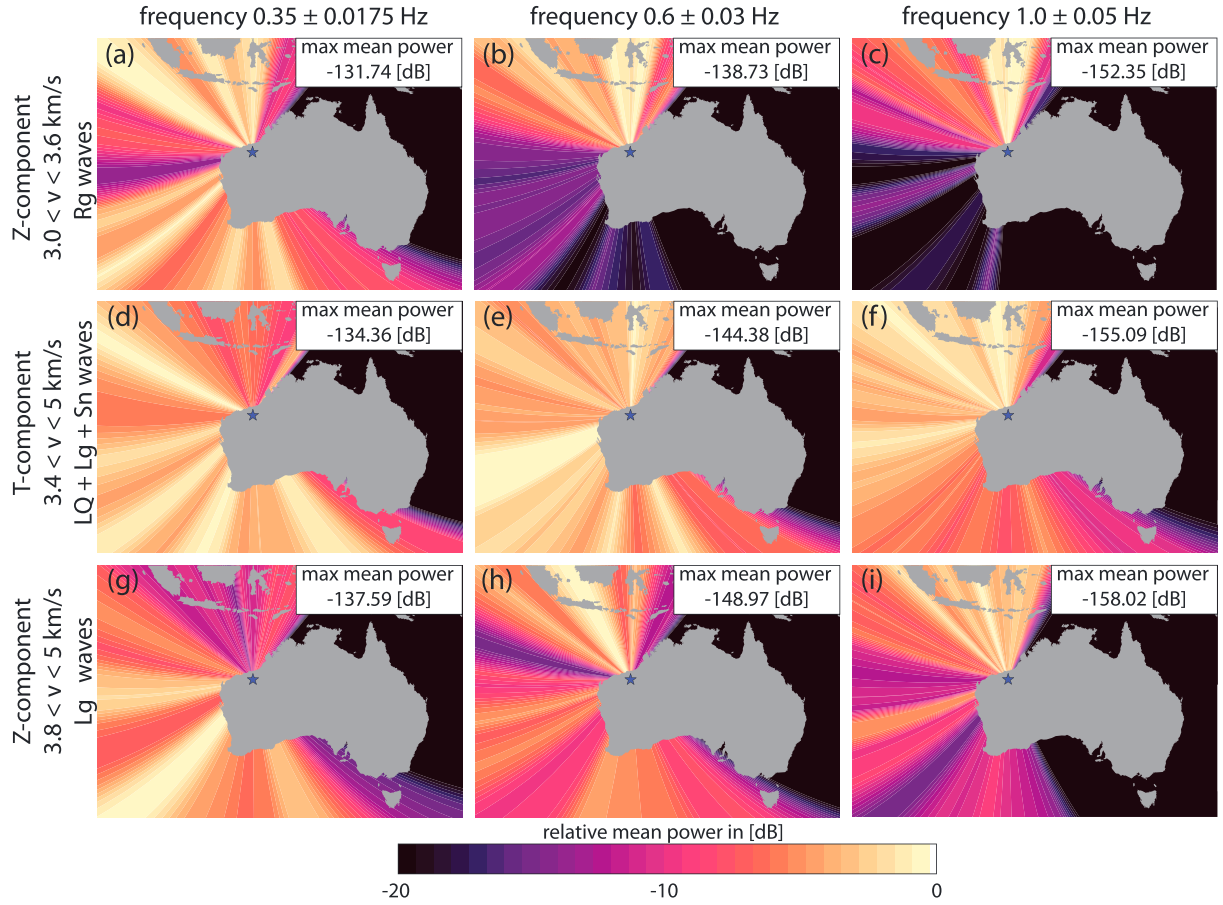

Figure 4. Projections of mean beam power toward the estimated direction of arrival for all of 2013. The figures are generated by taking all evaluated arrivals with CLEAN-3C, dividing the back azimuth into 5°-wide bins, and dividing the sum of all power in each bin by the number of hours processed, assuming that the raypaths follow great circle paths. Owing to the lack of arrivals at back azimuths of 40–125°, these directions are masked as they would not produce meaningful results. Each column represents one of the three frequency bands, and the first three rows show the estimated mean beam power for different wave types. Wave type, velocity, and component information are stated at the beginning of each row. The label "max mean power" represents the mean power of the strongest direction in each case.

component shows shallow *P* wave energy. Hence, CLEAN-3C reveals the underlying directional characteristics of the microseism spectrum that would otherwise be overshadowed by sidelobe energy.

Since CLEAN-3C decomposes the field into point sources, and the power contribution of each source is known and unbiased by sidelobe energy, the mean beam power representation can be reconstructed as a sum of all estimated CLEAN-3C power spectra. Discarding hours containing body wave earthquake energy is not necessary as *P* wave energy can be excluded from the summation of clean sources given their higher phase velocity. To exclude surface waves generated by earthquakes, we use the fact that microseismic energy varies relatively slowly from one hour to the next. If the summed power of radial/transverse surface wave energy exceeds an increase of 3 dB in comparison to the previous hour, the power spectrum is excluded from further analysis. This procedure has little effect on the vertical and radial power spectrum as little earthquake generated Rayleigh waves are found with PSAR but has a noticeable effect on the transverse component, where strong Love waves are found to originate from the northeast direction at higher frequencies.

We present the mean beam power of surface waves per hour (the hourly estimated clean beam power in m^2/s is averaged over the whole year) in Figure 4, for all three frequency bands, as outgoing rays from the array location. For this operation the back azimuth is discretized into 5° bins. Figures 4a–4c show R_g waves in the three frequency bands derived from the *Z* component for velocities $3.0 < v < 3.6$ km/s. We observe high beam power from the north, south, and west for the lowest frequency, $f_1 = 0.35$ Hz (Figure 4a). The directions with high mean beam power to the south are associated with convex coastline morphology. With increasing

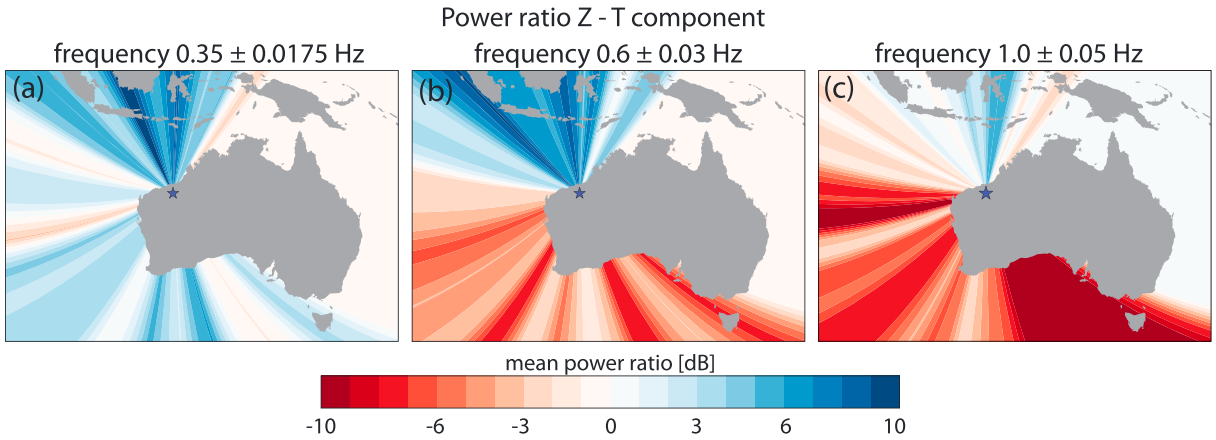

Figure 5. Power ratio between the *Z* and *T* components (for the *Z* component here we refer to $R_g + L_g$). The colormap levels are set from −10 dB to 10 dB; hence, values smaller or larger than these bounds are clipped with the maximal color. Clipping only occurs for the case in Figure 5c where the *T* component exceeds 10 dB (the arrivals from the SSE direction are up to −20 dB).

frequency, $f_2 = 0.6$ Hz and $f_3 = 1.0$ Hz, we see a strong reduction (by a factor of 10) in the average beam power from the south and west (Figures 4b and 4c). The reduction in power with increasing frequency matches well the increased attenuation expected for the high-frequency R_g waves traveling from more distant coastlines [e.g., *Mitchell*, 1995].

Beam power from the *T* component for $3.4 < v < 5$ km/s is shown in Figures 4d–4f for the three frequency bands. This result highlights transverse energy from *LQ*, L_g, and *Sn* phases. The *T* component results show some correlation with R_g for the case of f_1 (compare Figures 4a and 4d). The arrivals to the south do not fully align with the convex coastlines, but the power distribution to the west correlates well for the strongest beam directions. In general, we see smaller variation of mean power with respect to direction than for R_g, which shows stronger preference for certain back azimuths. For f_2 (Figure 4e), almost all directions (apart from the northeast to southeast where little to no signals are recorded) are within a mean beam power of 7 dB/h. We further observe a slight shift in the strongest beam directions on all coastlines. The strongest southern direction fits better with previously observed R_g directions at f_1 (Figure 4a). For f_3 (Figure 4f), the beam power from the south is reduced compared to directions for which the coastlines are closer. It should be noted that for the three frequency bands the strongest mean power direction of the *T* component is weaker than the estimated mean power of the strongest R_g direction (see differences in power between first and second rows in Figure 4).

For higher velocity ($3.8 < v < 5$ km/s) arrivals on the *Z* component (Figures 4g–4i), we observe predominantly L_g waves, which could include some contribution from higher mode R_g. As L_g is prominent on the vertical and transverse components, the results correlate to some degree with the results shown in Figures 4d–4f. The strongest mean power direction for f_1 is to the west and shifts to the north for f_2 and f_3. For f_3 and partially f_2, the L_g phase shows higher mean power to the south compared to the R_g phase, consistent with the lower attenuation of L_g.

We show the azimuthal variability in the ratio between *Z* and *T* component energy, for all three frequency bands, in Figures 5a–5c. The *Z*/*T* ratio in Figure 5 is displayed in decibels to make the scale linear and to readily show the large differences in power. Here we allow only surface waves with velocities <5.0 km/s. (Subdivision into R_g, *LQ*, and L_g is not feasible owing to the limited resolution of PSAR and the similarity in velocities.) The *Z*/*T* ratio at f_1 (Figure 5a) is in general positive for directions, where R_g waves show strong beam power, and negative for directions with low R_g beam power. At f_2 (Figure 5b) the effect of R_g attenuation/scattering is clearly visible as all directions from the south to west are dominated by *T* component energy. Only the coastlines north of PSAR that are in close proximity to the array display stronger mean vertical (R_g) beam power. For f_3 (Figure 5c), the R_g energy decreases further, and only a narrow swath of back azimuths to the north-northeast show a stronger vertical component. The *Z*/*T* power ratio integrated over all directions shows a notable decrease with increasing frequency: 1.95 for f_1, 1.86 for f_2, and 1.01 for f_3.

4. Discussion

4.1. Utility of CLEAN-3C

We have applied CLEAN-3C enhanced beamforming to 1 year of three-component seismic data recorded at PSAR. The analysis allows for the first full wavefield decomposition by means of a beamforming analysis, which enables an accurate comparison of slowness-dependent beam power for all separable wave phases. This gives us the ability to observe incoming microseismic energy from multiple sources, including weak sources, and determine the three-component motion of the incoming phases. We have utilized this new capability to compare the observed surface wave arrivals at PSAR and analyzed their generation mechanisms.

4.2. Detailed Comparison Between Surface Wave Phases

The results presented in this work show that vertical (R_g, L_g) and transverse (LQ, L_g) component surface waves are observed from all the coastlines of Australia except for the east coast, where attenuation effects owing to the long distance between source and array prevent their observation. R_g waves recorded on the Z component show a stronger azimuthal dependence compared to the LQ/L_g energy recorded on the T component. Previously reported directional similarities between R_g and LQ energy in the secondary microseism band [e.g., *Nishida et al.*, 2008; *Hadziioannou et al.*, 2012; *Behr et al.*, 2013] are partially present in our results, but deviations occur, especially for directions where R_g is weak. At the lowest frequency ($f_1 = 0.35$ Hz), we observe the Z component energy to be almost twice the strength of the T component; however, it is likely that Z/T ratios are regionally dependent especially for seismometers sited in sedimentary basins [*Koper and Burlacu*, 2015; *Juretzek and Hadziioannou*, 2016].

Attenuation and scattering of R_g play a key role for higher frequencies ($f_2 = 0.6$ Hz and $f_3 = 1.0$ Hz) and are consistent with observations that arrays located farther inland in central Australia (Warramunga and especially Alice Springs) are dominated by L_g from all directions [*Koper et al.*, 2010; *Gal et al.*, 2015]. The R_g/L_g ratios obtained for the three frequency bands, calculated from the Z component only, are 8.34, 9.00, and 2.76 for f_1, f_2, and f_3 respectively. The first two bands show a similar ratio, but strong reduction in the southern R_g energy is observed for f_2 when compared with f_1 (see Figures 4a and 4b); therefore, attenuation seems to be the main contributor for this reduction. The further decrease in directional R_g energy at f_3 suggests scattering from R_g to L_g [e.g., *He et al.*, 2008; *Gal et al.*, 2015] owing to the strong decrease in the R_g/L_g ratio at f_3. Given the characteristics of the higher attenuation/scattering of R_g waves for f_2 and f_3, it is safe to assume that this ratio is strongly dependent on the location of the array with respect to the closest coastline.

In Figure 6, we investigate the azimuthal variations in beam power in more detail and compare the R_g waves from the Z component with the mean power on the T component. For this analysis we focus on f_1, where the attenuation and scattering effects have the least impact and source excitation should be most important. The north facing coastline shows three directions with elevated R_g mean power levels (Figure 6a), which correspond well with the convex portions of the coastline. The T component (Figure 6b) shows a different picture as LQ waves are not generated by the same three convex segments of coastline. Instead, the location of LQ waves correlates with the Dampier Archipelago Islands north of the coast and a large sedimentary basin farther offshore (Figure 6g).

We make use of the "OZ SEEBASE" sedimentary thickness map (Figure 6g) developed by FROGTECH in 2005 and released in 2014 [*FROGTECH*, 2014]. The map was produced in collaboration with Geoscience Australia and covers Australia and offshore regions. The sediment thickness is derived as a subtraction between the Phanerozoic basement and the bathymetry. Hence, the sediment thickness is likely to include sedimentary rock and shows thicker layers of sediment compared to prior work [e.g., *Divins*, 2003]. Recent measurements of the seafloor sediment thickness in the southern Indian Ocean [*Whittaker et al.*, 2013] place increased sediment thickness in areas agreeing with the OZ SEEBASE and validate the spatial locations of sedimentary basins.

For the west facing coast (Figures 6c and 6d), the strongest azimuth for R_g and T component energy is identical and is found north and south of the Shark Bay area (Figure 1a). These directions also correlate with strong L_g directions (see Figure 4g). The Shark Bay area between the two prominent azimuths is known to be a seismic low-velocity zone [e.g., *Saygin and Kennett*, 2010, 2012]. Hence, the assumption of great circle path propagation is not appropriate and it is likely that the surface wave paths deviate at this location. The ratio between the T component and L_g from the Z component is close to 1 for these directions. Most of the transverse component power is therefore part of L_g and not LQ. Potentially, the topography of the Shark Bay area could contribute to the generation of L_g waves.

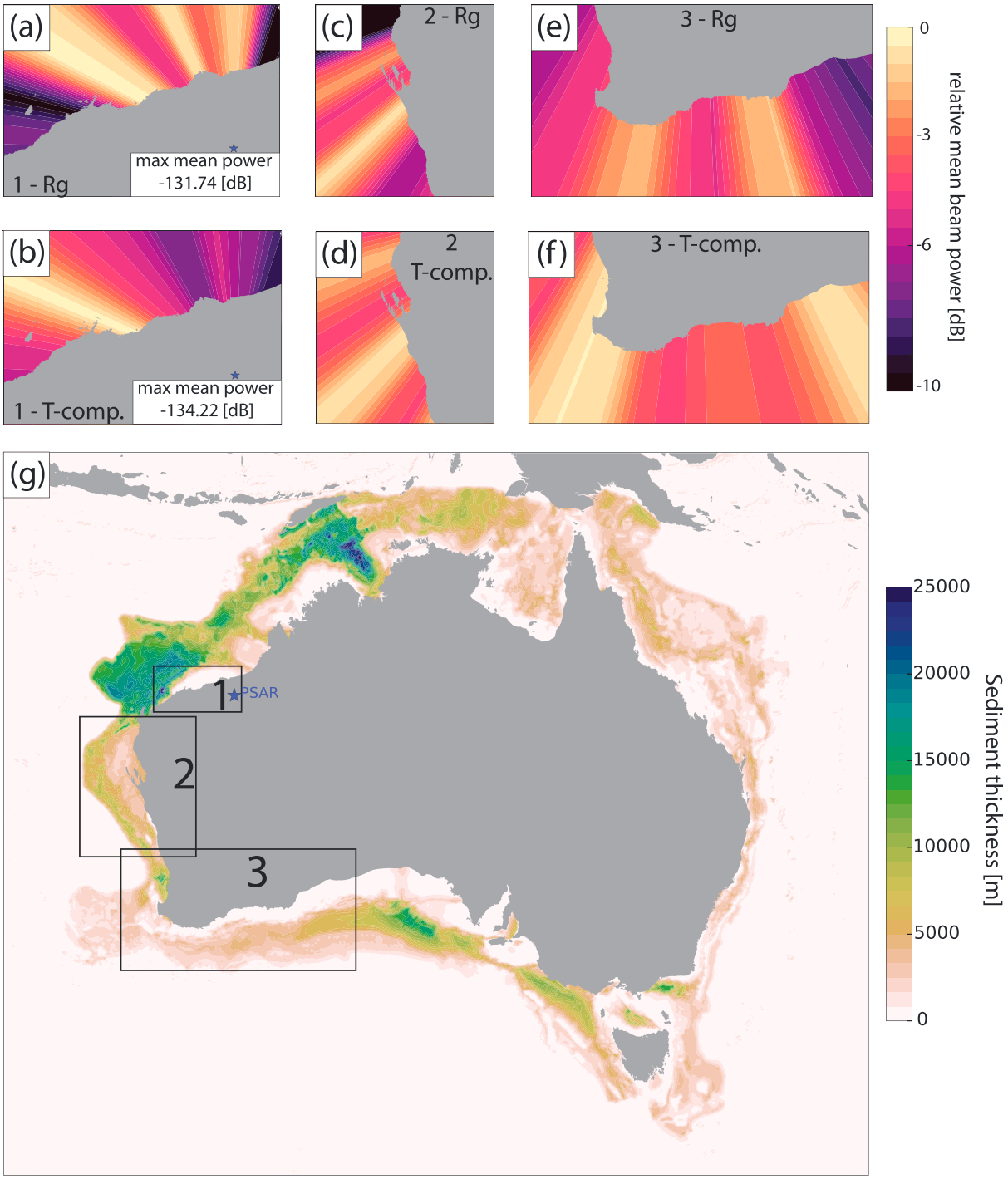

Figure 6. Zoomed regions from Figures 4a and 4d. (a, b) The northern, (c, d) the western, and (e, f) the southern coastlines for R_g waves and the T component are shown in the lowest frequency band, f_1. The colormap levels are identical to the values in Figures 4a and 4d for the R_g and T component case and shown here only for the case of the northern coastline. (g) The corresponding sediment thickness map OZ SEEBASE, product of *FROGTECH* [2014], also displays the zoomed geographical locations. Directions of strong *LQ* waves (Figures 6b and 6f) correlate well with thick seafloor sediment locations, while strong directions in (Figure 6d) are expected to be mainly L_g waves.

To the south (Figures 6e and 6f), the *LQ* waves are generated at different locations than R_g. Convex coastlines are again associated with azimuths of increased mean R_g energy. This suggests that convex coastlines either have a higher contribution to source excitation via coastline reflection or that the transfer function between land and ocean is more favorable. For *LQ*, we observe a different preferred azimuth that coincides with an increased thickness in seafloor sediments (Figure 6g). For a better understanding of our observations, we further compare them with the excitation predicted using synthetic source modeling.

4.3. Comparison Between Observation and Ocean Wave Model

The array analysis of surface waves has the limitation that their generation regions cannot be inferred by this method unless some type of triangulation is performed. With the improved understanding in synthetic source modeling of ocean-induced microseisms [*Ardhuin et al.*, 2011; *Ardhuin and Roland*, 2012; *Stutzmann et al.*, 2012; *Ardhuin and Roland*, 2012], a spatially dependent source excitation can be derived. We make use of the output from the WAVEWATCH III ocean model to obtain an estimate of the power spectral density of the equivalent surface pressure (available at the IFREMER ftp site as p2 l NetCDF files). With the knowledge of p2 l and an empirical seismic wave propagation model, the synthetic power distribution can be modeled for any seismic station [e.g., *Stutzmann et al.*, 2012]. To make the synthetic sources comparable to our array analysis, we average the p2 l value at each grid point for the full year 2013 and calculate the power spectrum of the vertical ground displacement in the oceans surrounding Australia as given in [*Ardhuin et al.*, 2011; *Stutzmann et al.*, 2012];

$$F_\delta(\lambda,\phi,f_s) = \frac{S_{DF}(f_s)}{R_E \sin\Delta} e^{\frac{-2\pi f_s \Delta R_E}{UQ}} P(f_s) \int_{-\pi/2}^{\pi/2}\int_0^{2\pi} R_E^2 \sin\phi' \,\mathrm{d}\lambda' \mathrm{d}\phi'. \tag{6}$$

The first term denotes the seismic source power spectral density $S_{DF}(f_s)$ at the double frequency $f_s = 2f$ divided by the geometrical spreading factor, where R_E is the Earth's radius and Δ the spherical distance between source and receiver. The second term describes the attenuation of each source and is governed by the product between group velocity U and quality factor Q. $P(f_s)$ is a frequency-dependent fitting parameter that adjusts the amplitude and accounts for variable site effects. The integral term denotes the surface area element for each source point (λ', ϕ'). The seismic source power spectral density is given as

$$S_{DF} \cong \frac{4\pi^2 f_s C}{\rho_s^2 \beta^5} F_{p3D}, \tag{7}$$

where C denotes the squared amplification coefficients as given in [*Longuet-Higgins*, 1950], $rho_s = 2600\,\mathrm{kg/m^3}$ is the crustal density, $\beta = 2800$ m/s denotes the *S* wave velocity, and F_{p3D} is equivalent to p2l.

The model is subject to certain approximations, which need to be considered for a quantitative comparison between model and observation. Modeling the synthetic ground displacement can be divided into two parts, the source excitation and the successive seismic energy propagation. The source excitation is a function of p2l, the reflection coefficient, and the sum of squared amplitude coefficients also known as ocean site effects (we disregard the constants here). Given that the bathymetry is fixed and the p2 l values are constrained by the ocean wave dynamics, errors are a direct result of the insufficient knowledge of the directional wave spectra and their modeling. The seismic energy propagation is in general poorly known and needs to be approximated with an empirical model. Hence, the path propagation effects are the largest uncertainty in the modeling process as they dictate the power contribution from a source at (λ', ϕ') and this should be taken into consideration for the following comparison between model and observations.

For a simple propagation model along the great circle paths with spatially constant $Q = 600$, $U = 1800$ m/s, and a coastal reflection coefficient of 10%, the synthetic displacement (calculated from the power spectral density) as modeled for PSAR can be calculated for the full year 2013. These values are chosen as a compromise between maximizing the correlation coefficient and minimizing the misfit value between model and observation [*Stutzmann et al.*, 2012]. In Figure 7a, we display the displacement for both cases of synthetic model and PSAR observations at 0.35 Hz. The correlation coefficient between to two functions yields 0.811, while the misfit is 0.224. Hence, this simple model reproduces the temporal displacement variation at PSAR sufficiently well. The source power which contributes to the modeled displacement at PSAR in this propagation model is displayed in Figure 7b. The strongest sources lie to the north of the array given the interplay between geometrical spreading, attenuation, ocean site effects, and p2l. To the west and south, a thin line of stronger excitation marks the bathymetry with preferential depth. The southern Indian Ocean shows contributions from deep water due to elevated p2 l values.

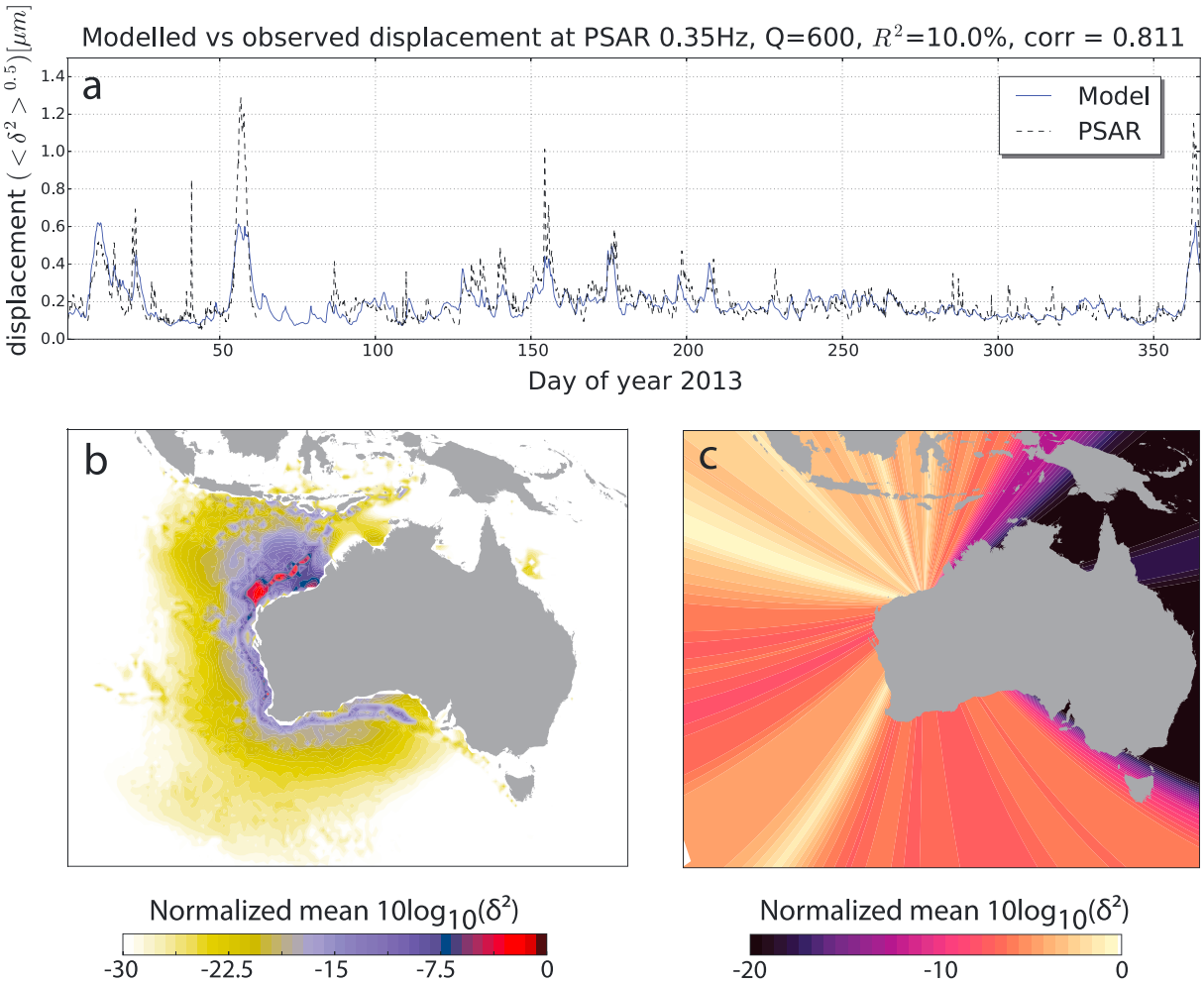

Figure 7. Synthetic source locations of secondary microseism R_g waves at 0.35 Hz, as observed from PSAR. (a) Modeled and observed displacements are shown for the duration of the year 2013 with a simple propagation model of constant $Q = 600$ and $U = 1800$ m/s. For the same propagation model, (b) the mean source power contribution for the full year. (c) The source power summed in 5° great circle path bins outgoing from PSAR, for a ready comparison with the beamforming observations. It should be noted that the synthetic model is in displacement squared and the array observations in velocity squared. In a narrow frequency range, the transformation between these two domains is linear; hence, a comparison between the model and array observations is possible. The normalization in Figure 7c compensated for the linear factor between the two domains.

To compare our observations to the model, we sum the power contributions as a function of back azimuth in 5° bins, as in the observed case. The result is shown in Figure 7c and represents the modeled displacement power for one possible propagation model. To the north, four azimuths with increased power are present. Three of them are present in our observed data in Figure 6a, while the farthest left is missing in the R_g results, but present in the *LQ* results (Figure 6b). The absence of this modeled source could be explained by the presence of sediments at the source area, which can strongly decrease the Rayleigh waves energy propagating toward land based stations [*Gualtieri et al.*, 2015]. The absence of R_g energy and strong presence of *LQ* energy hints at a potential coupling mechanism. It should be noted that coastline reflections in the model are required in order to model the three observed azimuths of increased mean power.

The northern part of the west coast shows little variation in modeled power and does not reflect the observed power distribution. This is likely due to path propagation effects not accounted for in this simple model as the Shark Bay area is subject to a low velocity zone. The southwestern and southern coasts show one strong azimuth which does not correlate with R_g observations (Figure 6e) but fits well with the *LQ* observations displayed in Figure 6f. This azimuth can be correlated with an increased seafloor sedimentary thickness that can potentially reduce R_g energy but does seem to favor the *LQ* energy.

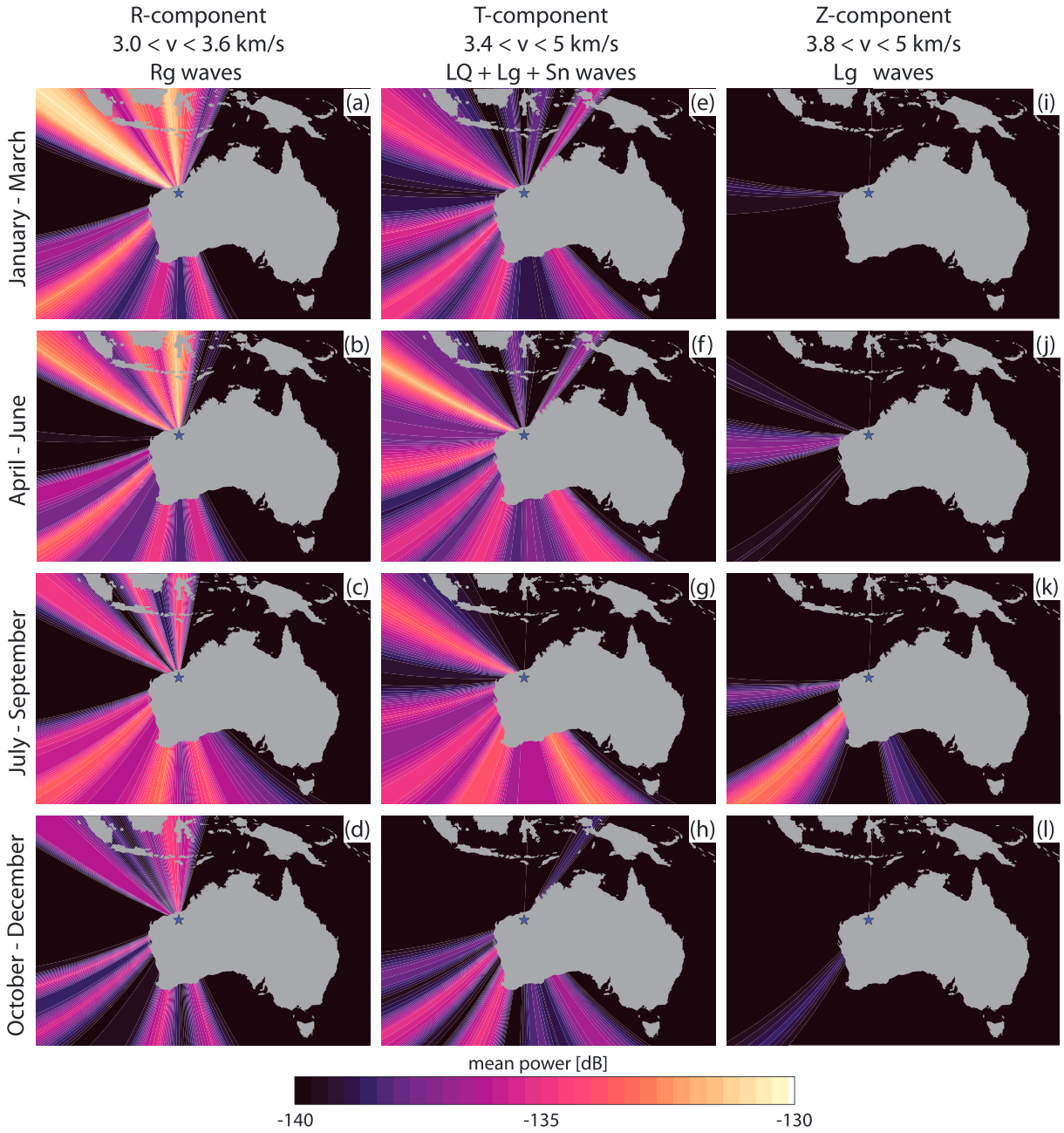

Figure 8. Seasonal mean power maps at 0.35 Hz (rows denote the seasonal quarters and columns display the respective wave type). The power is not normalized in this case to allow a direct comparison between components or wave types. The colorbar is set between −140 and −130 dB to better illustrate seasonal changes between the components. The R_g waves displayed in the first column are calculated from the R component (identical to Z component but closer in power to T component and L_g phase).

The absence of the observed R_g energy from the south can be attributed to the simplified propagation model. By adjusting group velocity and the quality factor for land and ocean separately, and a varying reflection coefficient, the model results in stronger energy from the south that better match the observations with a similar correlation coefficient and misfit value. We have experimented with modifying the model to the observational results, by constructing an empirical transfer function between model and observations, which increases or decreases the modeled power by an azimuthal dependent factor to match the observations. The model resulted in a correlation coefficient of 0.805 and misfit value of 0.219. This suggests that propagation effects such as focusing/defocusing, refraction, attenuation, and the transfer function between ocean and land need to be better known for an improved match between model and observation.

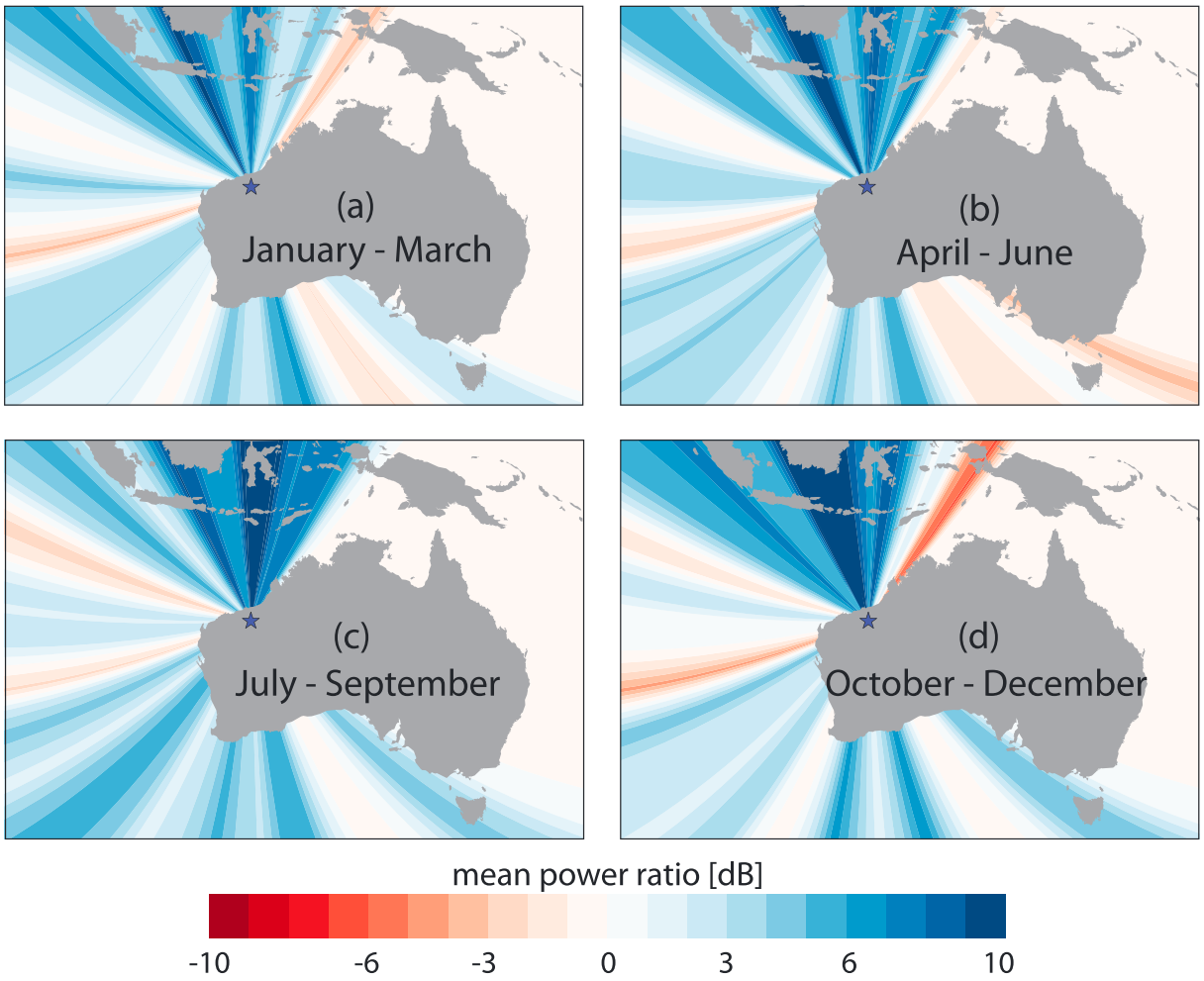

Figure 9. Seasonal *Z*/*T* ratio at 0.35 Hz. Colormap levels are as in Figure 5.

4.4. Generation of Love Waves

The generation of Love waves in the secondary microseism range is currently not fully understood. Previous research found Rayleigh and Love waves to originate from similar directions [e.g., *Friedrich et al.*, 1998; *Nishida et al.*, 2008; *Hadziioannou et al.*, 2012; *Behr et al.*, 2013], hence hinting at a similar source area. As potential candidates for their generation, coupling with the seafloor topography (e.g., seamount) or some type of scattering process have been suggested.

In our observations, we find distinct arrival azimuths for R_g and *LQ* waves and a more homogenized directional *LQ* distribution compared to R_g. This suggests that the oceanic wave-wave interaction, in combination with seamounts, is unlikely to be the only process responsible for the excitation of *LQ* waves; otherwise, R_g waves would be observed from these directions as well. When the *LQ* wave directions are compared to a sediment thickness map (Figure 6g), partial correlations are observed. Further support for this correlation is given by the synthetic model. Two of the strongest R_g azimuths predicted by the model, which coincide with thick seafloor sediments, show only little R_g energy but display strong *LQ* energy suggesting amplified excitation of seismic energy but simultaneous trapping of R_g energy [*Gualtieri et al.*, 2015]. Given the information provided by model and observation, it is likely that Love waves are generated via some mechanism at seafloor sedimentary basins.

LQ waves are known to be excited by *S* waves incident on sedimentary basin boundaries [e.g., *Kinoshita et al.*, 1992; *Hatayama and Fujiwara*, 1998] and hence could contribute to the observed *LQ* wavefield. It is yet to be determined if another mechanism contributes to the generation of *LQ* waves when interacting with a sediment layer. A potential candidate could be an R_g-to-*LQ* conversion, as *Hatayama and Fujiwara* [1998] showed

that the SV body waves can excite *LQ* waves at the sediment layer boundary. In a similar fashion, the SV component of R_g waves could potentially excite *LQ* waves. The amplified R_g energy could hence escape in the form of Love waves from the sedimentary basin. An R_g-to-*LQ* process could also explain the more homogenized directional *LQ* distribution as R_g waves excited in the ocean propagate in all directions [*Ardhuin et al.*, 2015] and conversion could occur at distant seafloor sedimentary basin boundaries, which are not directly exposed to oceanic wave-wave interactions.

4.5. Temporal Variations

The temporal variability of the microseismic wavefield at PSAR (here discussed for 0.35Hz but representative for the other two frequency bands as well) is governed by swell and wind sea activity of the southern Indian Ocean and displayed in Figure 8. The general preferred azimuths for each surface wave phase remain stationary for each quarter of the year 2013, but the respective mean power of each source location varies with time. The highest mean Rayleigh wave power is observed from January to March (Figure 8a), where elevated wind speeds due to sea breeze and a strong local storm at the end of February occur. The strongest southern arrivals are observed between July and September (Figure 8c), which is consistent with the elevated activity of the southern Indian Ocean. *LQ* waves show a similar behavior, although their strongest mean power from the north coast is observed in the second quarter. The northwest *LQ* direction shows higher mean power over R_g in the second and third quarters (Figure 8f and 8g). This is likely a result of the differing swell patterns in these quarters. In the first quarter, the main mean power contribution is generated by the strong local storm at the end of February. The storm develops south of Indonesia moving toward the location of PSAR from the north. This event predominantly excites R_g waves, while the observed energy of *LQ* waves is lower by a factor of 4 on average. In the second and third quarters, swells propagate northeast along the Australian west coast, which results in a stronger excitation of Love waves. Hence, the swell direction seems to impact the mean power of *LQ* waves. In the fourth quarter, where these swells rarely occur, very little Love wave excitation is observed from the northern coast and predominant R_g excitation occurs. L_g waves show an increase in the second and predominantly the third quarters, at times where more energetic swells are to be expected. The *Z*/*T* ratio remains relatively constant over the course of the year at 0.35 Hz, displayed in Figure 9, which is in agreement with recent finding for multiple European arrays [*Juretzek and Hadziioannou*, 2016]. For higher frequencies, the ratio decreases in the second and third quarters due to the increased southern Indian Ocean activity combined with the increased scattering/attenuation of R_g from southern directions.

5. Conclusion

We present the first 3C array study that decomposes the microseism wavefield in slowness space on each component and removes power contributions from beam sidelobes. The analysis accounts for the full power on each component and gives unprecedented azimuthal resolution on the excitation and propagation of high-frequency microseisms in Australia. It enables an accurate assessment of the power of R_g and L_g waves on the *Z* component and the surface wave portion of the *T* component (*LQ*, L_g), which is used to investigate the directional mean power ratios of these phases at distinct, different azimuths.

R_g waves are predominantly observed to coincide with convex portions of the coastlines at 0.35 Hz and experience increased attenuation/scattering with increasing frequency. Comparison with the WAVEWATCH III ocean model suggests the sources to be predominantly excited far away from coastlines, but coastline reflections are necessary to reproduce the observational results. *LQ* waves show limited correlation with R_g waves at 0.35 Hz as observed with beamforming. The synthetic source model suggests two strong R_g source azimuths, which are not present in the observations, given that the source areas are over deep sedimentary basins, where R_g energy is trapped. From these azimuths, elevated mean *LQ* energy is observed suggesting a transfer of R_g-to-*LQ* energy. For higher frequencies an increased correlation between R_g and *LQ* is observed, which is likely due to an increased proportion of the L_g phase on the *T* component. An influence of the swell direction on the *LQ* energy is also seen.

The mean beam power of the *Z* component is roughly twice as large as the *T* component for 0.35 and 0.6 Hz, and a strong directional difference between these two components can be observed. For 1 Hz, the power between *Z* and *T* is equal. These ratios remain constant in each quarter of the year at 0.35 Hz, and vary for higher frequencies due to the increased attenuation/scattering of R_g waves and the higher activity of the southern Indian Ocean. We observe the strongest arrivals from the north in the first quarter, which are due to tropical cyclone activity. The southern Indian Ocean shows highest activity in the third quarter.

Acknowledgments
We acknowledge Geoscience Australia as operators of PSAR and data access through the IRIS DMC. We thank the Tasmanian Partnership for Advanced Computing (TPAC), which enabled the access to its HPC Facilities. We are grateful to Fabrice Ardhuin for useful discussion and comments regarding the IFREMER implementation of the WAVEWATCH III ocean model. We acknowledge support from/discussions within TIDES COST Action ES1401. The manuscript has been improved by comments from two anonymous reviewers and the Editor. Funded by the Australian Research Council under project DP150101005. M.G. is supported through a Tasmanian Government Research Scholarship. K.D.K. and R.B. acknowledge support from NSF-EarthScope under award EAR-091558. CLEAN-3C code is freely available and may be obtained by contacting the University of Tasmania authors.

References

Ardhuin, F., and A. Roland (2012), Coastal wave reflection, directional spread, and seismoacoustic noise sources, *J. Geophys. Res.*, *117*, C00J20, doi:10.1029/2011JC007832.

Ardhuin, F., E. Stutzmann, M. Schimmel, and A. Mangeney (2011), Ocean wave sources of seismic noise, *J. Geophys. Res.*, *116*, C09004, doi:10.1029/2011JC006952.

Ardhuin, F., L. Gualtieri, and E. Stutzmann (2015), How ocean waves rock the Earth: Two mechanisms explain microseisms with periods 3 to 300 s, *Geophys. Res. Lett.*, *42*, 765–772, doi:10.1002/2014GL062782.1.

Behr, Y., J. Townend, M. Bowen, L. Carter, R. Gorman, L. Brooks, and S. Bannister (2013), Source directionality of ambient seismic noise inferred from three-component beamforming, *J. Geophys. Res. Solid Earth*, *118*, 240–248, doi:10.1029/2012JB009382.

Chevrot, S., M. Sylvander, S. Benahmed, C. Ponsolles, J. M. Lefèvre, and D. Paradis (2007), Source locations of secondary microseisms in western Europe: Evidence for both coastal and pelagic sources, *J. Geophys. Res.*, *112*, B11301, doi:10.1029/2007JB005059.

Divins, D. (2003), *Total Sediment Thickness of the World's Oceans & Marginal Seas*, NOAA Natl. Geophys. Data Cent., Boulder, Colo.

Euler, G. G., D. Wiens, and A. A. Nyblade (2014), Evidence for bathymetric control on the distribution of body wave microseism sources from temporary seismic arrays in Africa, *Geophys. J. Int.*, *197*(3), 1869–1883, doi:10.1093/gji/ggu105.

Friedrich, A., K. Klinge, and F. Krüger (1998), Ocean-generated microseismic noise located with the Graefenberg array, *J. Seismol.*, *2*(1), 47–64.

FROGTECH (2014), Phanerozoic OZ SEEBASE v2 GIS. Bioregional Assessment Source Dataset. [Available at: http://data.bioregionalassessments.gov.au/dataset/26e0fbd9-d8d0-4212-be52-ca317e27b3bd.]

Gal, M., A. M. Reading, S. P. Ellingsen, L. Gualtieri, K. D. Koper, R. Burlacu, and H. Tkalčić (2015), The frequency dependence and locations of short-period microseisms generated in the Southern Ocean and west Pacific, *J. Geophys. Res. Solid Earth*, *120*, 5764–5781, doi:10.1002/2015JB012210.

Gal, M., A. M. Reading, S. Ellingsen, K. D. Koper, R. Burlacu, and S. J. Gibbons (2016), Deconvolution enhanced direction of arrival estimation using one- and three-component seismic arrays applied to ocean induced microseisms, *Geophys. J. Int.*, *206*(1), 345–359, doi:10.1093/gji/ggw150.

Gerstoft, P., P. M. Shearer, N. Harmon, and J. Zhang (2008), Global *P*, *PP*, and *PKP* wave microseisms observed from distant storms, *Geophys. Res. Lett.*, *35*, L23306, doi:10.1029/2008GL036111.

Gualtieri, L., E. Stutzmann, Y. Capdeville, V. Farra, A. Mangeney, and A. Morelli (2015), On the shaping factors of the secondary microseismic wavefield, *J. Geophys. Res. Solid Earth*, *120*, 6241–6262, doi:10.1002/2015JB012157.

Hadziioannou, C., P. Gaebler, U. Schreiber, J. Wassermann, and H. Igel (2012), Examining ambient noise using colocated measurements of rotational and translational motion, *J. Seismol.*, *16*, 787–796, doi:10.1007/s10950-012-9288-5.

Hasselmann, K. (1963), A statistical analysis of the generation of microseisms, *Rev. Geophys.*, *1*(2), 177–210.

Hatayama, K., and H. Fujiwara (1998), Excitation of secondary Love and Rayleigh waves in a three-dimensional sedimentary basin evaluated by the direct boundary element method with normal modes, *Geophys. J. Int.*, *133*, 260–278, doi:10.1046/j.1365-246X.1998.00477.x.

Haubrich, R., W. Munk, and F. Snodgrass (1963), Comparative spectra of microseisms and swell, *Bull. Seismol. Soc. Am.*, *53*(1), 27–37.

Haubrich, R. A., and K. McCamy (1969), Microseisms: Coastal and pelagic sources, *Rev. Geophys.*, *7*(3), 539–571.

He, Y., X.-B. Xie, and T. Lay (2008), Explosion-source energy partitioning and *Lg*-wave excitation: Contributions of free-surface scattering, *Bull. Seismol. Soc. Am.*, *98*(2), 778–792, doi:10.1785/0120070119.

Juretzek, C., and C. Hadziioannou (2016), Where do ocean microseisms come from? A study of Love-to-Rayleigh wave ratios, *J. Geophys. Res. Solid Earth*, *121*, 1–16, doi:10.1002/2016JB013017.

Kedar, S., M. Longuet-Higgins, F. Webb, N. Graham, R. Clayton, and C. Jones (2008), The origin of deep ocean microseisms in the North Atlantic Ocean, *Philos. Trans. R. Soc. London, Ser. A*, *464*(2091), 777–793, doi:10.1098/rspa.2007.0277.

Kennett, B. L. N., J. Stipčević, and A. Gorbatov (2015), Spiral-arm seismic arrays, *Bull. Seismol. Soc. Am.*, *105*(4), 2109–2116, doi:10.1785/0120140354.

Kinoshita, S., H. Fujiwara, T. Mikoshiba, and T. Hoshino (1992), Secondary Love waves observed by a strong-motion array in the Tokyo Lowlands, Japan, *J. Phys. Earth*, *40*(1), 99–116, doi:10.4294/jpe1952.40.99.

Koper, K. D., and R. Burlacu (2015), The fine structure of double-frequency microseisms recorded by seismometers in North America, *J. Geophys. Res. Solid Earth*, *120*, 1677–1691, doi:10.1002/2014JB011820.

Koper, K. D., B. de Foy, and H. Benz (2009), Composition and variation of noise recorded at the Yellowknife Seismic Array, 1991–2007, *J. Geophys. Res.*, *114*, B10310, doi:10.1029/2009JB006307.

Koper, K. D., K. Seats, and H. Benz (2010), On the composition of Earth's short-period seismic noise field, *Bull. Seismol. Soc. Am.*, *100*(2), 606–617, doi:10.1785/0120090120.

Landès, M., F. Hubans, N. M. Shapiro, A. Paul, and M. Campillo (2010), Origin of deep ocean microseisms by using teleseismic body waves, *J. Geophys. Res.*, *115*, 1–14, doi:10.1029/2009JB006918.

Liu, Q., K. D. Koper, R. Burlacu, S. Ni, F. Wang, C. Zou, Y. Wei, M. Gal, and A. M. Reading (2016), Source locations of teleseismic *P*, *SV*, and *SH* waves observed in microseisms recorded by a large aperture seismic array in China, *Earth Planet. Sci. Lett.*, *449*, 39–47, doi:10.1016/j.epsl.2016.05.035.

Longuet-Higgins, M. (1950), A theory of the origin of microseisms, *Philos. Trans. R. Soc. London, Ser. A*, *243*(857), 1–35.

Mitchell, B. J. (1995), Anelastic structure and evolution of the continental crust and upper mantle from seismic surface wave attenuation, *Rev. Geophys.*, *33*(95), 441–462, doi:10.1029/95RG02074.

Nishida, K., and R. Takagi (2016), Teleseismic *S* wave microseisms, *Science*, *353*(6302), 919–921, doi:10.1126/science.aaf7573.

Nishida, K., H. Kawakatsu, Y. Fukao, and K. Obara (2008), Background Love and Rayleigh waves simultaneously generated at the Pacific Ocean floors, *Geophys. Res. Lett.*, *35*, L16307, doi:10.1029/2008GL034753.

Obrebski, M., F. Ardhuin, E. Stutzmann, and M. Schimmel (2013), Detection of microseismic compressional (*P*) body waves aided by numerical modeling of oceanic noise sources, *J. Geophys. Res. Solid Earth*, *118*, 4312–4324, doi:10.1002/jgrb.50233.

Reading, A. M., K. D. Koper, M. Gal, L. S. Graham, H. Tkalčić, and M. A. Hemer (2014), Dominant seismic noise sources in the Southern Ocean and West Pacific, 2000–2012, recorded at the Warramunga Seismic Array, Australia, *Geophys. Res. Lett.*, *41*, 3455–3463, doi:10.1002/2014GL060073.

Roueff, A., P. Roux, and P. Réfrégier (2009), Wave separation in ambient seismic noise using intrinsic coherence and polarization filtering, *Signal Process.*, *89*(4), 410–421, doi:10.1016/j.sigpro.2008.09.008.

Roux, P. (2009), Passive seismic imaging with directive ambient noise: Application to surface waves and the San Andreas Fault in Parkfield, CA, *Geophys. J. Int.*, *179*(1), 367–373, doi:10.1111/j.1365-246X.2009.04282.x.

Saito, T. (2010), Love-wave excitation due to the interaction between a propagating ocean wave and the sea-bottom topography, *Geophys. J. Int.*, *182*(3), 1515–1523, doi:10.1111/j.1365-246X.2010.04695.x.

Saygin, E., and B. L. N. Kennett (2010), Ambient seismic noise tomography of Australian continent, *Tectonophysics*, *481*(1–4), 116–125, doi:10.1016/j.tecto.2008.11.013.
Saygin, E., and B. L. N. Kennett (2012), Crustal structure of Australia from ambient seismic noise tomography, *J. Geophys. Res.*, *117*, 1–15, doi:10.1029/2011JB008403.
Schimmel, M., E. Stutzmann, F. Ardhuin, and J. Gallart (2011), Polarized Earth's ambient microseismic noise, *Geochem. Geophys. Geosyst.*, *12*, 1–14, doi:10.1029/2011GC003661.
Shapiro, N. M., and M. Campillo (2004), Emergence of broadband Rayleigh waves from correlations of the ambient seismic noise, *Geophys. Res. Lett.*, *31*(7), L07614, doi:10.1029/2004GL019491.
Stutzmann, E., F. Ardhuin, M. Schimmel, a. Mangeney, and G. Patau (2012), Modelling long-term seismic noise in various environments, *Geophys. J. Int.*, *191*(2), 707–722, doi:10.1111/j.1365-246X.2012.05638.x.
Tanimoto, T., C. Hadziioannou, H. Igel, J. Wasserman, U. Schreiber, and A. Gebauer (2015), Estimate of Rayleigh-to-Love wave ratio in the secondary microseism by colocated ring laser and seismograph, *Geophys. Res. Lett.*, *42*, 2650–2655, doi:10.1002/2015GL063637.
Tanimoto, T., C. Hadziioannou, H. Igel, J. Wassermann, U. Schreiber, A. Gebauer, and B. Chow (2016), Seasonal variations in the Rayleigh-to-Love wave ratio in the secondary microseism from colocated ring laser and seismograph, *J. Geophys. Res. Solid Earth*, *121*, 2447–2459, doi:10.1002/2016JB012885.
Toksöz, M., and R. Lacoss (1968), Microseisms: Mode structure and sources, *Science*, *159*, 872–873.
Traer, J., P. Gerstoft, P. D. Bromirski, and P. M. Shearer (2012), Microseisms and hum from ocean surface gravity waves, *J. Geophys. Res.*, *117*(B11307), doi:10.1029/2012JB009550.
Wagner, G. (1996), Resolving diversly polarized, superimposed signals in three-component seismic array data, *Geophys. Res. Lett.*, *23*(14)1837–1840.
Wagner, G., and T. Owens (1996), Signal detection using multi-channel seismic data, *Bull. Seismol. Soc. Am.*, *86*(1A), 221–231.
Whittaker, J. M., A. Goncharov, S. E. Williams, R. D. Müller, and G. Leitchenkov (2013), Global sediment thickness data set updated for the Australian-Antarctic Southern Ocean, *Geochem. Geophys. Geosyst.*, *14*, 3297–3305, doi:10.1002/ggge.20181.
Zhang, J., P. Gerstoft, and P. M. Shearer (2009), High-frequency *P*-wave seismic noise driven by ocean winds, *Geophys. Res. Lett.*, *36*, L09302, doi:10.1029/2009GL037761.